Geomechanics for Energy and the Environment 35 (2023) 100489

Contents lists available at ScienceDirect

Geomechanics for Energy and the Environment

journal homepage: www.elsevier.com/locate/gete

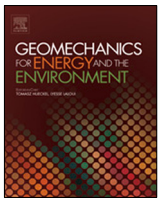

The physics of desiccation cracks 2: Modeling and prediction of the crack patterns

Ruoyu Chen *, Winston Lindqwister, Fei Wu, Boleslaw Mielniczuk, Tomasz Hueckel, Manolis Veveakis

Civil and Environmental Engineering, Duke University, Durham, 27708, NC, USA

ARTICLE INFO

Article history:
Received 15 May 2023
Accepted 11 July 2023
Available online 18 July 2023

Editors-in-Chief:
Professor Lyesse Laloui and Professor Tomasz Hueckel

Keywords:
Desiccation cracks
Rate sensitivity
Viscoplasticity

ABSTRACT

This paper extends the experimental results of our companion paper by modeling and predicting the onset and pattern formation of desiccation cracks in geomaterials (Ruoyu et al., 2023). Thin-layer silt samples in controlled atmospheric conditions were tested to obtain the surface strain maps with the digital image correlation (DIC) method during dehydration. Support experiments, including consolidation and displacement-controlled triaxial tests, were conducted for the properties of geomaterials. These experimental results were used to validate a viscoplastic theoretical model by comparing cracks and singularities locations that distribute following the Cnoidal wave pattern. A critical value exists in the viscoplastic model that determines the number of singularities, which accurately predicts the number of cracks in the experiment. The critical values contain two crucial parameters: rate sensitivity and λ. Rate sensitivity describes the rate-dependent stress–strain relation, while λ shows the ability of pore pressure redistribution under the external mechanical loading rate. These results provide a new view to analyze the desiccation cracks considering the rate-dependent viscoplasticity.

1. Introduction

The shrinkage caused by desiccation is essential in many infrastructures, from road building and tunnel construction to nuclear waste disposal.[1–4] The reduction of cracks, or at least mitigation, is the key to reducing the potential damage. However, the mechanism of cracking during desiccation is still far from fully comprehended.

One of the most common failure methods in desiccation cracking is tensile stress failure, in which cracks appear when effective tensile stress overcomes the tensile strength.[5] Three origins likely caused the exceedance of effective stress to the tensile strength, including the friction caused by boundary conditions, stress concentration inside the geomaterials, and inhomogeneous structure.[6,7] As the effective stress in the geomaterial is hard to measure directly, the surface images were captured and analyzed by the DIC method to discuss the desiccation cracks.[8] Based on the strain map generated by DIC, a strain-rate-dependent model, which indicates the plastic strain changes with the stress in the rheology relationship, is given to describe the plastic deformation in the geomaterials.[9,10] One crucial criterion to validate the theoretical model is the prediction of failure patterns in which the distribution of surface cracks is easy to obtain. Peron showed cracks were parallel distributed along the surface for the long thin layer samples and cracks intersecting between 90° and 150° on the square slabs.[7] Similar results were found with different geomaterials and dimensions by other researchers.[11,12] Another criterion is the correlation between the existence and number of cracks from experiments and theoretical models, which requires more analysis.

Motivated by the consistency between the theoretical pattern from the viscoplastic model and the experimental dehydration tests presented in our companion paper,[13] the atmospheric conditions controlled experiments were conducted on a thin layer basal constraint platform to obtain the parameters and check the accuracy of the theoretical model proposed by Ref. 14. The controlled atmospheric conditions, temperature and relative humidity, provide the reference stress and background volumetric strain rate. And the consolidation and triaxial tests give the consolidation coefficient and rate sensitivity. The theoretical model used the parameters from the experiment to predict the pattern and number of failures, which was compared with desiccation cracks in the experiment.

* Corresponding author.
E-mail address: ruoyu.chen@duke.edu (R. Chen).

https://doi.org/10.1016/j.gete.2023.100489
2352-3808/

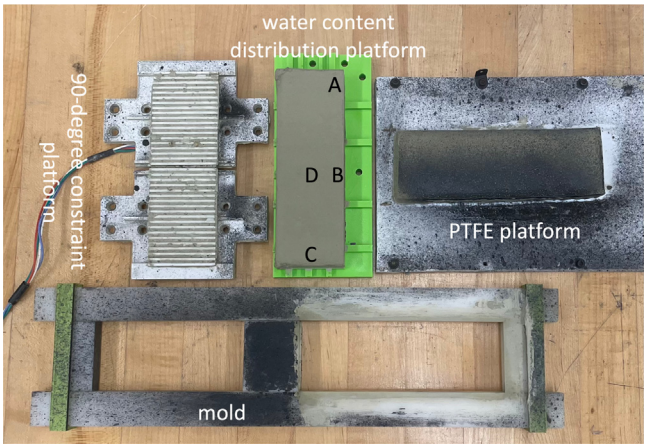

Fig. 1. The mold and different types of basal platforms. On the water content distribution platform, point A is the corner, point B is the mid-length, point C is the mid-width, and point D is the center.

2. Methodology

2.1. Materials and setup

The geomaterial used in the experiments is granite silt powder, whose characteristics are shown in Table 1. The powder and distilled water mixture were thoroughly stirred by a spatula and left undistributed on the table for 30 min for the homogeneous water content. The initial water contents, which are gravimetric in this paper, of the saturated samples in the tests are 33 ± 3%. Shown in Fig. 1, a mold was used to shape the material to the desired dimensions: 150 mm × 50 mm × 14 mm (*length* × *width* × *depth*). The inside of the mold was covered by polytetrafluoroethylene (PTFE) strips and coated with lubrication oil for minimal friction during the molding process. The bottom of the samples is located on a 90-degree angular constraint platform. Meanwhile, another group was processed on a PTFE platform coated with lubrication oil in the same atmospheric conditions to determine the crack generation conditions. And the sample surfaces were sprayed with black paint to increase the contrast, increasing the accuracy of the results from the DIC.

All experiments were conducted in an atmospheric condition-controlled chamber shown in Fig. 2. Four sensors were installed to monitor the temperature and relative humidity in the chamber. The values from three sensors, except sensor A, were shown on the outside panel, whose average values were compared with the desired value. When the humidity in the chamber is higher than the set value, the fans located at the silica gel and the tube entrance activate to reduce the humidity. In contrast, when the humidity value on the panel is lower than the set value, the humidifier in the water tank is activated in conjunction with the fans at the water tank and entrance of the tube to increase the humidity. The air conditioner controlled the temperature set to 25 ± 1 °C in the tests. The initial atmospheric conditions converge to the desired value based on these humidity and temperature adjustments during the test, which were monitored and recorded by sensor A.

Two Canon EOS 4000D cameras were installed on the aluminum framework inside the chamber, one above the constraint plates and the other above the PTFE plate. These cameras capture the samples' surface images every 1 min. DIC software is used to process these surface images.[15] The original photos were rotated and cropped in XnViewMp software to obtain rectangle surface images shown in Fig. 3. The image series was selected from the processed surface images, starting from several minutes before crack onset till the end of cracking. The region of interest (ROI) on the surface images meshes into circles. And the movements of circle centers between the reference image (first image) and the "current" image (image at each minute) were determined and used to calculate the strain development on the surface.

Table 1
Physical properties of the geomaterial.

Specific gravity	Liquid limit	Plastic limit	Poisson's ratio
2.892	25.02%	17.15%	0.2857
Young's modulus	Shear modulus	Consolidation coefficient	
8.6 MPa	3.3 MPa	1.82 mm^2/s	

A highly sensitive moisture analyzer, RAD WAG MA 50/1.R., measures the initial water contents with the leftover geomaterials right after molding. A precision mass balance, Adventurer Pro AV812C with 0.01 g readability, is installed under the test samples to record the weight changes during the desiccation test every 10 s in the atmospheric chamber.

The difference in surface areas between each side may cause the inhomogeneous water content distribution inside the thin layer samples. So, the water content distribution experiments were conducted to determine the water contents at different locations on the surface. Six samples were molded and laid on the same none-constraint platform in one group. For one sample in the group, we picked pieces (2 ± 1 g) located at the corner, mid-length, mid-width, and center to measure the water content values as shown in Fig. 1. The sensitive moisture analyzer measured the water contents of these pieces. And six samples were measured at different times. The time intervals between each measurement vary from 2 to 10 h, depending on different evaporation stages and relative humidity.

The odometer test was conducted to obtain the consolidation coefficient of geomaterials.[16] In the consolidation test, five different pressures (54, 107, 214, 429, and 858 kPa) were applied to the sample. And the value shown in Table 1 is selected as the average value of the consolidation coefficient calculated from t_{90}.

Beyond the desiccation and consolidation test, the displacement-controlled triaxial test was conducted to obtain the rate sensitivity of the geomaterial. The diameter of the cylinder sample is 34.55 mm, and the height is 75.37 mm. The initial axial loading rate is 0.5 mm/min. Once the stress reaches the ultimate stress, different loading rates are applied for the changes in the ultimate stress, which gives the rate sensitivity based on the rheology relation between strain rates and ultimate deviatoric stress.

2.2. Mathematical modeling

The top surface images of thin layer samples were captured and selected as ROI (Fig. 3). In the model formulation setup, we treat the sign convention of the static and kinematic fields as invariant and analyze the sample as purely volumetric compaction and dilatational bars.

The stress equilibrium between effective stress and fluid pressure in this 2D problem is

$$\frac{\partial p'}{\partial x_i} = \frac{\partial p^f}{\partial x_i} \tag{1}$$

where p' is effective stress, p^f is fluid pressure, x_1 is the X direction and x_2 is the Y direction. Then the momentum balance equations are

$$\frac{\partial \sigma_{x_i}}{\partial x_i} = 0 \tag{2}$$

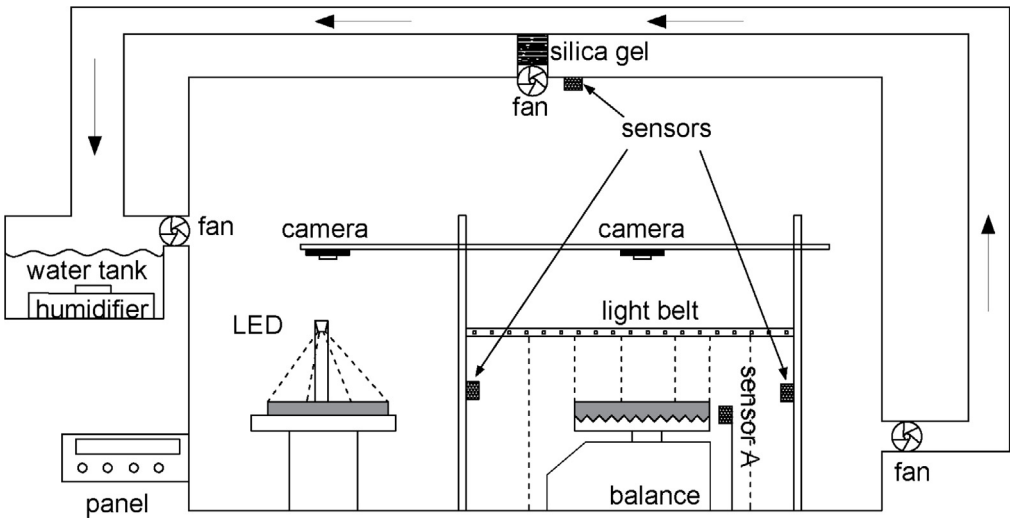

Fig. 2. The atmospheric chamber with humidity controllers. The left sample lies on the PTFE plate; the right sample lies on the platform with constraints; the panel controls and monitors the humidity based on three sensors; the sensor next to the sample, sensor A, records atmospheric conditions and sends data to the connected laptop.

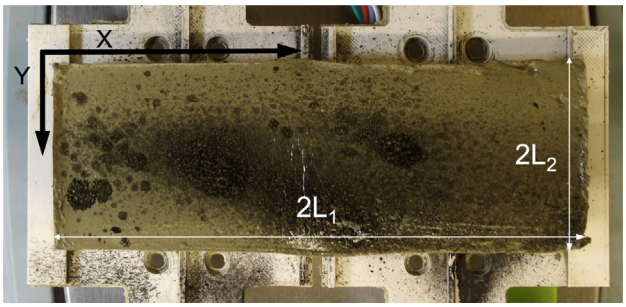

Fig. 3. The setup of the dimension ($2L_1 \times 2L_2 \times H$)used in the discussion.

where σ_{x_i} is orthogonal normal stress along x_i direction. The concept of partial density in a bi-phasic material gives us the density for solid phase, $\rho^1 = (1-\theta)\rho_s$ and fluid phase density, $\rho^2 = \theta\rho_f$, which provides the mass balance as:

$$\frac{\partial \rho^\alpha}{\partial t} + \frac{\partial \rho^\alpha v^\alpha_{x_i}}{\partial x_i} = 0 \tag{3}$$

in which ρ_s, ρ_f are solid skeleton and fluid density, θ is porosity, and $v^\alpha_{x_i}$ is the barycentric velocity ($\alpha = 1$ for solid phase; $\alpha = 2$ for fluid phase) in x_i direction. With the assumption that the solid and fluid are incompressible, ρ_s and ρ_f are treated as constant.[17,18] Then the mass balance for solid and fluid phases can be shown as follows:

$$\frac{\partial (1-\theta)}{\partial t} + \frac{\partial (1-\theta) v^1_{x_i}}{\partial x_i} = 0 \tag{4}$$

$$\frac{\partial \theta}{\partial t} + \frac{\partial \theta v^2_{x_i}}{\partial x_i} = 0 \tag{5}$$

Superposing the mass balance equations in different phases. The mass balance equation for the geomaterial sample is

$$\frac{\partial \theta (v^2_{x_i} - v^1_{x_i})}{\partial x_i} + \frac{\partial v^1_{x_i}}{\partial x_i} = 0 \tag{6}$$

where $(v^2_{x_i} - v^1_{x_i})$ is the relative velocity of the fluid to the matrix.[19] We followed the relation between the relative velocity and compaction rate and Darcy's law[17]:

$$\theta(v^2_{x_i} - v^1_{x_i}) = -\frac{k_\pi}{\mu_f}\frac{\partial p^f}{\partial x_i} \tag{7}$$

where k_π is the permeability, and μ_f is the fluid viscosity. As the permeability and viscosity are hard to measure without disturbance samples during the desiccation experiment, the reference consolidation coefficient equals:

$$c'_v = \frac{k_\pi}{\mu_f} \tag{8}$$

And volumetric strain rate is defined as:

$$\dot{\epsilon_v} = \frac{\partial v^s_{x_i}}{\partial x_i} \tag{9}$$

The volumetric strain rate in the geomaterial has two parts: a linear elastic part, which is reversible ($\dot{\epsilon^r_v}$), and a plastic part following standard power-law rheology, which is irreversible ($\dot{\epsilon^i_v}$):

$$\dot{\epsilon_v} = \dot{\epsilon^r_v} + \dot{\epsilon^i_v} \tag{10}$$

$$\dot{\epsilon^r_v} = \frac{\dot{p'}}{K} \tag{11}$$

$$\dot{\epsilon^i_v} = \dot{\epsilon_n}\left[\frac{\bar{p'}}{p'_n}\right]^m \tag{12}$$

where $\dot{p'}$ is the rate of effective stress, K is the soil elastic bulk modulus, $\dot{\epsilon_n}$ is the reference volumetric strain rate (background loading rate), $\bar{p'} = \langle p' - p'_y \rangle$ is the effective overstress, p'_y is the yield stress, p'_n is the reference stress, and m is the rate sensitivity exponent for geomaterials.[20,21] As the paper searches for the crack distribution method instead of the propagation process, the steady-state equation is deduced instead of transient equations, where $\dot{p'} = 0$.[20,22] The steady-state allows treating the volumetric strain rate as pure plastic. Substituting Eqs. (7)–(12), the Eq. (6) can be rewritten as:

$$c'_v \frac{\partial^2 p'}{\partial x_i^2} = \dot{\epsilon_n}\left[\frac{\bar{p'}}{p'_n}\right]^m \tag{13}$$

which has the dimensionless form:

$$\frac{\partial^2 \sigma'}{\partial z_i^2} - \lambda \sigma'^m = 0 \tag{14}$$

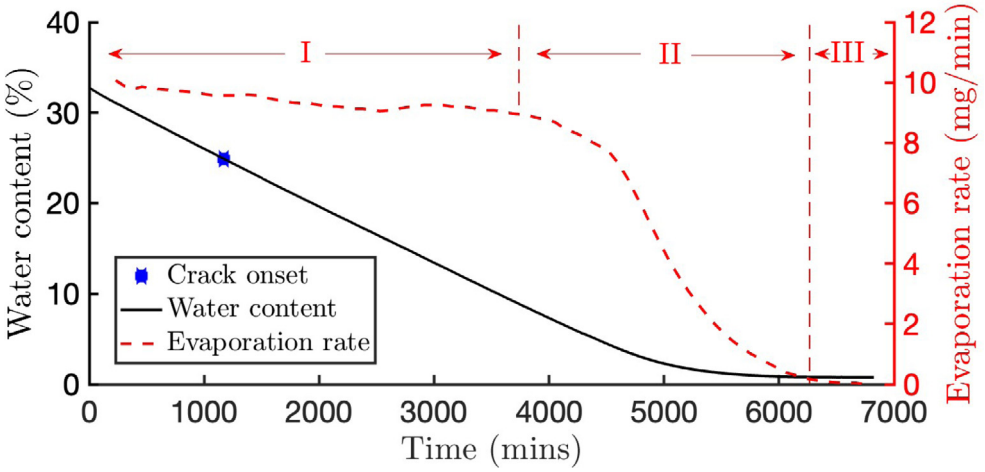

Fig. 4. Water content and evaporation rate development on the 90-degree constraint platform with 85% humidity. The crack initiated at 1170 min (the black marker). Stage I is the constant evaporation rate stage; Stage II is the falling evaporation rate stage; Stage III is the residual evaporation rate stage.

with dimensionless parameters:

$$\sigma' = \frac{\bar{p}'}{p'_n} \qquad z_i = \frac{x_i}{2L_i} \qquad \lambda = \frac{\dot{\epsilon_n}}{p'_n c'_v}(2L_i)^2 \tag{15}$$

where L_i is half length ($i = 1$) or width ($i = 2$) of the sample. The boundary conditions are $\sigma' = 1$ when $z_i = 0$ and $z_i = 1$, indicating the value of reference stress equals the effective stress on the side surfaces.

3. Results

3.1. Sample homogeneity

The deformation in desiccation is the shrinkage mechanically generated by the effective stresses. The fluid pressure, specified as suction here, is caused by the molecular scale's Laplace and capillary pressure, whose value is highly related to the water content.[23–25] As one predominant factor used to interpret effective stress, the water content needs to be discussed in the desiccation process. Meanwhile, the water content distribution is required to ensure the inhomogeneity of water content does not trigger failure and check the permission to treat the sample as homogeneous in the theoretical model.

The desiccation process is split into three stages based on the variation of evaporation rates: (I) constant rate stage, (II) falling rate stage, and (III) residual rate stage.[26,27] Fig. 4 shows the results from the test with 85% relative humidity and 25 °C temperature on the 90-degree constraint platform. In Stage I (0 min–3650 min), the water content decreases from 32.5% to 9.5%, while the evaporation rate is a constant that equals 9.3 mg/min. In the second Stage (3650 min–6365 min), the evaporation rate decreases from 9.3 mg/min to 0.1 mg/min while the water content jumps to 0.78%. In Stage III (6365 min - end), the change of evaporation rate ceased, and the value is less than 3×10^{-4} mg/min^2. In this stage, water content stays around 0.78%. Two cracks appeared and propagated during the first evaporation stage (constant rate stage) in all constraint experiments.

As the evaporation happens at the fluid–vapor contact surface, the difference in contact surface area at four points on the sample surface can influence the water loss mass rate as follows:

$$\begin{aligned}
\partial \dot{m}^{\gamma}_{evap} &= J \cdot \partial S^{\gamma}_{lv} \\
\partial S^{A}_{lv} &= \partial x \partial y + \partial x \partial z + \partial y \partial z \\
\partial S^{B}_{lv} &= \partial x \partial y + \partial x \partial z \\
\partial S^{C}_{lv} &= \partial x \partial y + \partial y \partial z \\
\partial S^{D}_{lv} &= \partial x \partial y
\end{aligned} \tag{16}$$

where $\dot{m}^{\gamma}_{evap}$ is the evaporation rate at different points, J is flux, S^{γ}_{lv} is liquid–vapor contact surface area, and γ is A, B, C, D respectively correspond to the points A, B, C, D on the samples shown in Fig. 3. The thin layer samples used in these experiments provided a simplification, $\int \partial z \ll \int \partial x$, that provided a uniform water content distribution with constant flux. Water contents at four different points on one sample were simultaneously measured. And the times of measurements in the test with 75% relative humidity were at 0, 300 min, 1200 min, 1560 min, 1800 min, 2580 min, and 2940 min (see Fig. 5).

The initial water contents at all points are 31.29%. At 300 min, the average water content is 29.19% and the maximum water content difference is 0.55% between point A and point D. At 1200 min, the average water content is 23.65%, and the maximum water content difference is 1.15% between point A and point B. At 1560 min, the average water content is 18.81% and the maximum water content difference is 0.4% between point B and point D. At 1800 min, the average water content is 16.76%, and the maximum water content difference is 0.86% between point A and point D. At 2580 min, the average water content is 9.16% and the maximum water content difference is 1.15% between point C and point D. At 2940 min, the average water content is 8.86%, and the maximum water content difference is 0.75% between point A and point B. The maximum water content variation is 12.5% at 2580 min, which is in the residual rate stage. In the period from start to the crack onsets, 0–1560 min in this test, the maximum water content variation is 4.86%, which allows treating water contents in the geomaterial as homogeneous distribution during our interest period (from the start of the test till the end of cracking).

3.2. Reference volumetric strain rate and reference stress

The shrinkage volume goes through three stages in dehydration: normal shrinkage stage, residual shrinkage stage, and no shrinkage stage.[28] Cracks initiate in the normal shrinkage stage, where the volume changes at a constant velocity. Fig. 6 shows the movement of the edges in the 90-degree constraint test by the DIC method in 76% relative humidity, and temperature is 24 °C. The series of images in the DIC method starts at 1212 min and ends at 1380 min, during which one crack was discovered.

Cracks paralleling the Y direction are found in the desiccation tests. In the image series, the edges in the Y direction shrank constantly and were not disrupted by the appearance of the crack. And the edge movement in the X direction initially had a linear

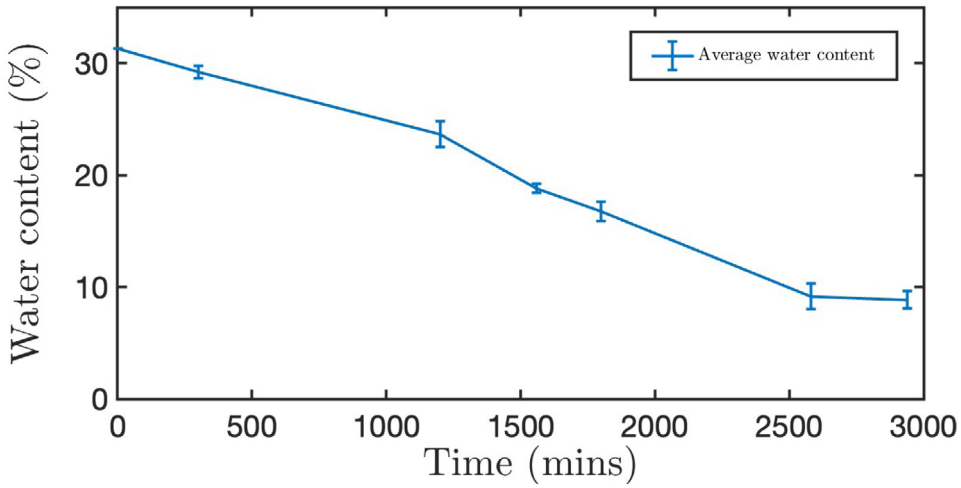

Fig. 5. Average water contents development and maximum water content variation between different points in the water distribution test;.

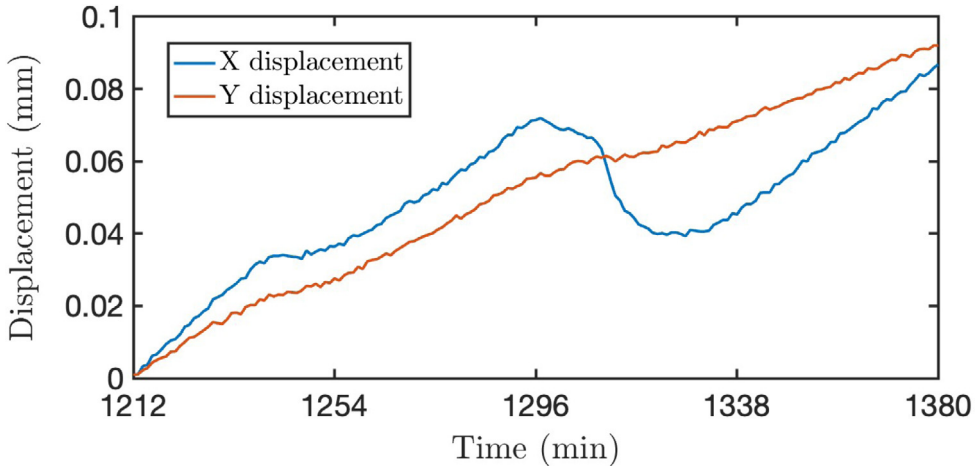

Fig. 6. Edge displacement in X and Y direction from 1212 min to 1380 min in basal constraint test with 76% humidity.

stage till a jump caused by the crack generation, followed by another linear part.

The total shrinkage volume is the summation of the product between edge movement and corresponding surface area with different side surfaces. The linear portion from 1212 min to 1232 min in Fig. 6 was select to calculate the background loading rate, which is the volumetric strain rate in Eq. (9). This period avoids the rapid volume changes caused by the generation of cracks and gives the rate in the normal shrinkage stage.

In the X direction, the edge movement velocity is 1.20×10^{-3} mm/min, and the corresponding surface area is 1400 mm^2. In the Y direction, the edge movement velocity is 6.02×10^{-4} mm/min, corresponding with a surface area equal to 4200 mm^2. The summation of the shrinkage volume rate in the X and Y directions is 0.0701 mm^3/s, referring to the volumetric strain rate from sides as 6.68×10^{-7}/s.

Meanwhile, the mass change caused by evaporation was measured by the precise mass balance. And the evaporation volume rate can be calculated based on the mass changes following the formulation:

$$\dot{\epsilon}_w = \frac{\dot{m}_{evap}}{\rho_w v_t} \tag{17}$$

where ρ_w is water density, v_t is total volume, 105 cm^3, and $\dot{m}_{evap}$ is 1.64×10^{-4} g/s in the test with 76% relative humidity. Then the total evaporation volumetric strain rate is 1.55×10^{-6}/s.

The correlation between the shrinkage volume in X and Y directions from the DIC method and the total evaporation volume from the balance exists a gap: the lack of deformation in the Z direction in the DIC method. The evaporation mass through side surfaces in X and Y directions is invoked to cover this gap. In a stable atmospheric condition, the evaporation flux is constant, meaning the evaporation mass from each surface depends on the surface areas. As water cannot evaporate from the bottom surface, the ratio of evaporation mass from the side surface to the total evaporation mass equals the side surface area to the side surface areas plus the top surface area, which is 0.4275. Then the evaporation volume rate only from the side surface is 6.63×10^{-7}/s.

The deviation of the volumetric strain rate calculated from DIC and the value calculated based on mass changes is 0.75%, which confirms the accuracy of using the evaporation rate to calculate the volumetric strain rate. This proves the volume changes in the normal shrinkage stage are water evaporation volume. The evaporation rates with different humidities are shown in Fig. 7, illustrating the volumetric strain rates change with relative humidity following Eq. (18).

$$\dot{\epsilon}_n = -4.4 \times 10^{-9} \times RH + 4.97 \times 10^{-7} \tag{18}$$

which gives the reference volumetric strain rates in different relative humidities.

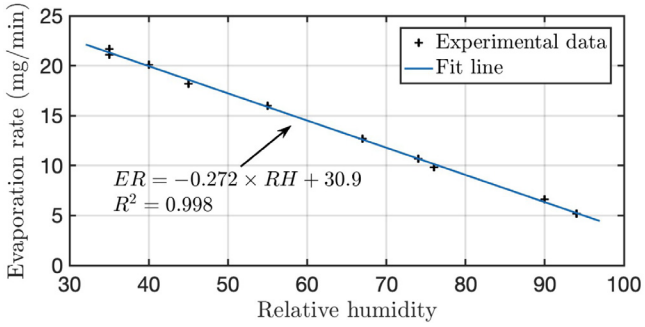

Fig. 7. Evaporation rates in different relative humidities. The evaporation rates were obtained from the constant evaporation rate stages. The negative linear relation between evaporation rate and relative humidities provides a way to calculate reference volumetric strain rates.

The reference stress in Eq. (15) equals the effective stress on the side surfaces, which is determined by the relative humidity for simplification. The definition of relative humidity is the ratio of the partial pressure of water vapor in the air to the saturation vapor pressure.[29] With the constant saturation vapor pressure, the effective stress on the sides in different relative humidity has the following empirical formula:

$$p_n' = -0.9506 \times RH + 110.4 \tag{19}$$

3.3. Consolidation coefficient and rate sensitivity

The consolidation coefficient from the odometer test provides a reference value for the c_v' in different experiments. As shown in Eq. Eq. (8), the consolidation coefficient changes based on the permeability and fluid viscosity of the geomaterial. In desiccation tests with different relative humidities, the type of fluid and temperature are the same indicating a constant viscosity in all the experiments. However, the permeability has fluctuation resulting from different void ratios as[30]:

$$k_\pi = k_0 \frac{e^3}{1+e} \tag{20}$$

where k_0 depends on the specific surface area and the shapes of pores, and e is the void ratio at crack onsets. The solid volume can be calculated from the mass of the solid. The void volume in the normal shrinkage stage is the initial total volume minus the shrinkage volume and solid volume. And the shrinkage volume is obtained from the evaporation rate and crack onsets. The calculated values of the void ratio are shown in Table 2. Then the consolidation coefficient is adjusted as follows:

$$c_v' = c_0 \frac{e^3}{1+e} \tag{21}$$

where c_0 is the consolidation coefficient from the odometer test shown in Table 1.

The rate sensitivity, as a property of the material, is measured from the triaxial test. Different ultimate deviatoric stresses are found with varying loading rates with the same confining stress. Results from the triaxial tests are shown in Fig. 8. When the axial strain rate increases from 0.000663/s to 0.0133/s, the ultimate deviatoric stress increases from 1253 kPa to 1293 kPa. Based on Eq. (12), the rate sensitivity of this geomaterial used in the viscoplastic model is 94.

3.4. Morphology

The morphology of the cracks in the desiccation is discussed, including the pattern of and distance between cracks. The cracks

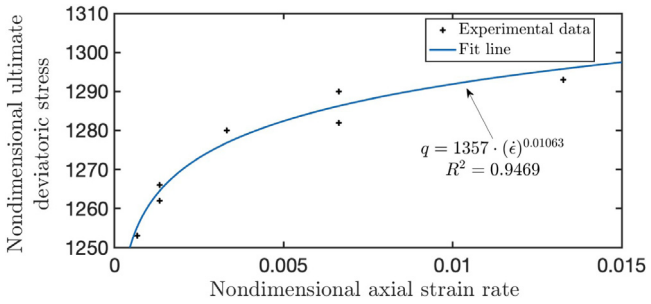

Fig. 8. The nondimensional ultimate deviatoric stress in the triaxial test with different non-dimensional axial loading rates.

are only found in the surface images from the constraint experiment, while no cracks are observed on the PTFE platform. Fig. 9 (a1), (b1), and (c1) show the original surface images respectively correspond to the sample without cracks, with one and two cracks. The image at 1212 min is selected as the reference image (the first image in the image series) in the DIC analysis, and the strain maps (a2), (b2), and (c2) are images taken at 1222 min, 1247 min, and 1362 min.

The 90-degree constraint platform prevents shrinkage in the X direction, while the sample can still freely shrink along the Y direction. As a result of the constraint, cracks are found perpendicular to the X-axis. After the initiation of instability, the crack develops along the Y direction and suspends when the cracks develop to the edges. Strain distributions along the mid-white lines are selected to determine the singularity locations considering the symmetry along the Y direction. Two positive peaks of ϵ_{xx} in Fig. 9.(c3) represent the locations of two cracks, and the horizontal distance between peaks is the distance of cracks.

Before the generation of crack (Fig. 9.(a3)), both ϵ_{xx} and ϵ_{yy} is in the magnitude of 10^{-4} at the location of the potential crack. As shown in (b3), the magnitude of ϵ_{xx} increases to 10^{-2} with ϵ_{yy} in the magnitude of 10^{-4}. With further development found in (c3), ϵ_{xx} at first and second cracks has the same magnitude of 10^{-2} with corresponding ϵ_{yy} have value of 10^{-3} at the first crack and 10^{-4} at the second crack. The magnitude difference between ϵ_{xx} and ϵ_{yy} gives the simplification only to consider the strain along the X direction, which simplifies Eq. (14) into a 1D formulation.

Different signs of the strain were found in the strain maps, where the positive sign represents expansion and the negative means shrinkage. ϵ_{yy} has a negative sign along the middle line in the whole period in the image series, indicating continuous shrinkage in the Y direction. Meanwhile, ϵ_{xx} has both positive and negative values. In the X direction, one positive strain concentration point appears at the crack initiation location, surrounded by two negative strain concentration areas at the left and right sides, which is the typical pattern of tensile failure.

4. Discussion

The experimental results and theoretical prediction were compared to check the accuracy of the viscoplastic model. Instead of focusing on the value of stress, the spacing between and the number of stress peaks is discussed. The number of cracks is the number of singularities in Eq. (14), while the spacing between cracks can be found as the distance of different singularities from the viscoplastic model. The equidistant distance between cracks from the model is shown as follows[14]:

$$d_{cal} = m^{-\frac{1}{4}} \sqrt{\frac{\lambda_0}{\lambda_{cal}}} \tag{22}$$

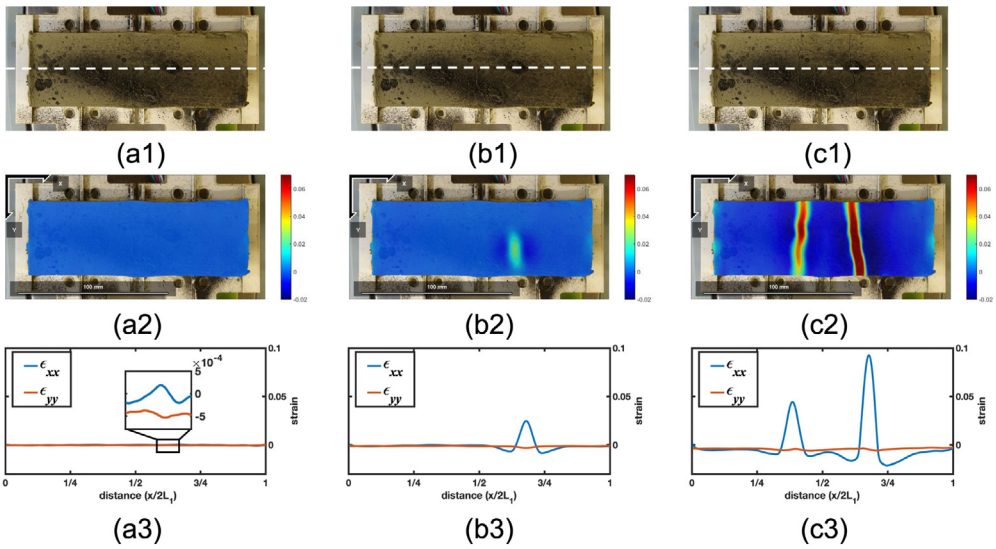

Fig. 9. Surface images from the desiccation process on the 90-degree constraint platform with 76% relative humidity. The reference image is taken at 1212 min, and Δt with reference image is 10, 35, and 150 min for the images in groups (a), (b), and (c); (a2), (b2), and (c2) are ϵ_{xx} strain maps from DIC analysis; (a3), (b3), and (c3) refer the ϵ_{xx}, ϵ_{yy} along the mid white line.

Table 2
Details of the experimental results.

Exp ID	Relative humidity (%)	Void ratio at crack onset	Number of cracks	Water content at crack onset (%)	Experimental crack distance (d_{exp})	Theoretical crack distance (d_{cal})
1	35	0.896	2	25.3	0.331	0.299
2	35	0.864	2	24.4	0.246	0.286
3	40	0.973	2	24.8	0.330	0.333
4	45	0.882	2	24.7	0.342	0.294
5	55	0.817	2	24.0	0.276	0.268
6	67	0.883	2	23.3	0.317	0.298
7	74	0.981	2	25.8	0.312	0.342
8	76	0.907	2	24.4	0.268	0.311
9	90	0.867	2	23.9	0.290	0.301
10	94	0.904	2	26.3	0.366	0.321

where d_{cal} is distance between cracks, $\lambda_0 = 12.7$ is constant, and λ_{cal} is calculated from Eq. (15). The reference volumetric strain rate is derived from Eq. (18), the reference stress on the sides comes from Eq. (19), and the consolidation coefficient is adjusted based on different void ratios.

Fig. 10 compares the distance from the theoretical model and the experiments. The deviation between predicted and experimental results may come from the void ratio variation. As a time-independent model, Eq. (14) is able to describe the stress distribution along the surface as a stationary state, where the void ratio is treated as constant. When cracks appear, the void volume sharply increases, and the evaporation rate can no longer represent the shrinkage volume rate. Despite the deviation from the void ratio, the distance between cracks by prediction is in accord with the experimental space. This consistency suggests that the pattern of cracks is, instead of randomly distributed in pure elastic materials, following the Cnoidal wave distribution. When stress is applied to the boundaries, a portion of the stress homogeneously transfers the whole sample as the elastic stress wave, and the leftover stress only partially transmits in the sample due to the viscoplasticity.[31,32] The superposition of viscoplastic and elastic waves gives the preferred Cnoidal wave pattern of crack distribution.

One question emerges in the Cnoidal wave analysis: how to determine the number of peaks. For the simplified 1D desiccation test in this paper, the critical values (λ_{cr}) are introduced to predict the number of cracks, which are shown as[14]:

$$\lambda_{cr} = \lambda_0 {N_s}^2 e^{-0.0175m} \tag{23}$$

where N_s is the number of cracks. For the sample with n cracks, λ should be above the λ_{cr} ($N_s = n$) and below λ_{cr} ($N_s = n+1$). Fig. 10 shows λ_{cal} from Eq. (15). λ_{cal} locate above 9.81 (critical value for two cracks) and below 22.1 (critical value for three cracks). To prevent the generation of failure, λ_{exp} needs to locate in the narrow range of critical values between $N_s = 0$ and $N_s = 1$, which can be realized by a shorter sample. When the length becomes smaller, the boundary influence needs to be considered, and the samples cannot be treated as the simplified 1D model but 2D tensile model where polygonal cracks will be found.[14] On the contrary, the sample with a bigger length may be found with more cracks.

We do perform experiments on the same geomaterial with different dimensions (300 mm × 50 mm × 14 mm). However, the void ratios were not obtained due to the lack of initial mass, and relative humidities were not recorded in these old generations of tests. Due to the drawback, λ_{exp} were calculated inverse from the crack distance as:

$$\lambda_{exp} = \frac{\lambda_0}{{d_{exp}}^2 m^{\frac{1}{4}}} \tag{24}$$

The median value of crack distances was selected to calculate the λ_{exp} for the tests with more than two cracks. When the length-to-width ratio increases from 3 to 6, the crack numbers increase as well and become 4 to 7. Fig. 11 shows that values of λ_{exp} calculated from the experiment are precisely in the range between the critical value from n cracks and $n+1$ cracks. The critical values indicate the existence of the maximum number

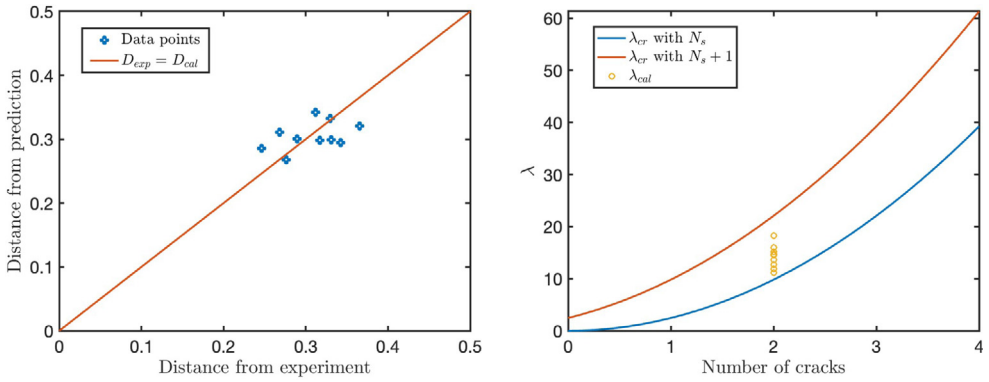

Fig. 10. Distance between cracks from experiment results and theoretical prediction(left); λ_{cal} from the viscoplastic model and the critical values with different numbers of cracks(right).

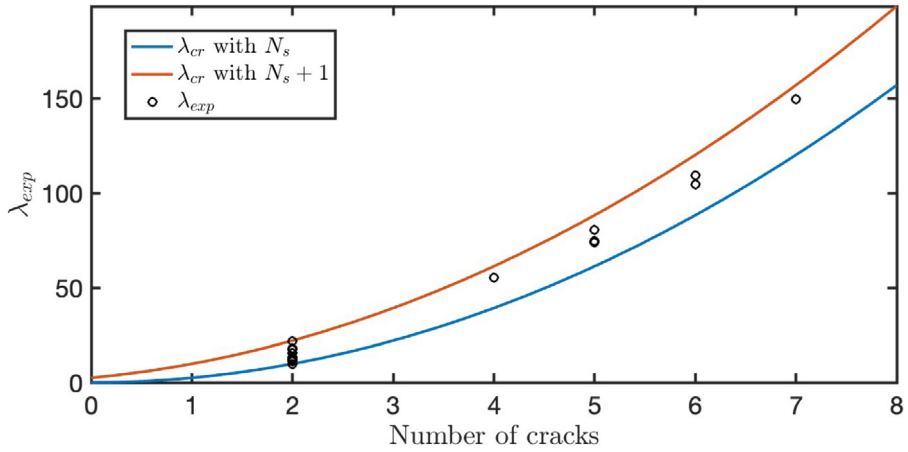

Fig. 11. λ_{exp} calculated based on crack distance and critical values with different numbers of cracks.

of cracks in the simplified 1D sample in desiccation. Based on the property of the samples and the atmospherical conditions, the maximum of λ can be calculated, which locates between the critical values from N_{max} and $N_{max} + 1$.

Now the physical meaning of λ needs to be discussed. Recalling the formulation from Eq. (15), λ describes the mechanical volumetric deformation rate ($\dot{\epsilon_n} \cdot 2L_1 \cdot 2L_2 \cdot H$) under the redistribution of external force on the side surfaces and the shrinkage ability along the middle line ($\frac{p'_n \cdot c'_v \cdot 2L_2 \cdot H}{2L_1}$), where the shrinkage ability is replaced by consolidation coefficient.[14] And the bifurcation between λ and λ_{cr} can be interpreted as a competition between external mechanical loading rate and internal matrix redistribution. Once the loading rate exceeds the capacity of the geomaterials, cracks are formed, resulting in the increment of the void ratio. Then the sample has the ability to adjust the external mechanical shrinkage rate, and the cracking process is suspended.

5. Conclusions

Constraint desiccation experiments in different relative humidities were performed with thin-layer samples. Valuable information on geomaterials, including the shrinkage rate, rate sensitivity, and consolidation coefficient, were obtained from the DIC test, triaxial experiment, and consolidation tests. These factors were applied to the viscoplastic theoretical model proposed by Veveakis,[14] and the primary outcomes are drawn as follows:

- Desiccation has three evaporation rate stages, and crack onsets appear in the constant rate stage. Meanwhile, the shrinkage volume rate is constant from the start to crack onsets, known as the normal shrinkage stage. The consistency between the shrinkage volume calculated from the DIC method and the evaporation volume measured by the balance confirms the accuracy of using the evaporation rate to calculate shrinkage volume in the normal shrinkage stage. The evaporation rate shows a clear negative linear relationship with the relative humidity, representing the volumetric strain rate changes with the relative humidity.
- The viscoplastic model describes the stress distribution along the surface, where singularities represent crack locations. In the simplified 1D model, the locations of stress singularities distribute following the Cnoidal wave formation for the rate-sensitive materials ($m > 1$). The crack distance can be predicted based on the geomaterials' properties (rate sensitivity, void ratio, permeability, and dimension) and external conditions(relative humidity). The predicted distance between cracks shows an agreement with the experimental results, proving the validity of the viscoplastic model.
- Critical values of λ were found corresponding with different numbers of cracks and the type of geomaterial. N_s cracks will be observed if λ from experiment locates in the range of critical values with N_s and $N_s + 1$ cracks. For the same geomaterials under the same atmospheric conditions, more cracks are found with longer samples as a result of λ increment. On the contrary, when the length decrease, two types of results exhibit: one is fewer cracks, and the other is cracking in polygon shape instead of parallel distribution when the geomaterial cannot be simplified as the 1D sample.

CRediT authorship contribution statement

Ruoyu Chen: Analysis, Manuscript wrote, Data analyses. **Winston Lindqwister:** Software. **Fei Wu:** Methodology. **Boleslaw Mielniczuk:** Methodology. **Tomasz Hueckel:** Supervision, Funding acquisition. **Manolis Veveakis:** Supervision, Conception of the study, Funding acquisition.

Declaration of competing interest

The authors declare that they have no known competing financial interests or personal relationships that could have appeared to influence the work reported in this paper.

Data availability

Data will be made available on request.

Acknowledgments

The authors gratefully acknowledge the support of the U.S. Department of Energy, United States grant DE-NE0008746 and the U.S. National Science Foundation for project CMMI-2042325.

References

1. Rajeev P, Kodikara J. Numerical analysis of an experimental pipe buried in swelling soil. *Comput Geotech*. 2011;38(7):897–904.
2. Gourc J, Camp S, Viswanadham B, Rajesh S. Deformation behavior of clay cap barriers of hazardous waste containment systems: Full-scale and centrifuge tests. *Geotext Geomembr*. 2010;28(3):281–291. http://dx.doi.org/10.1016/j.geotexmem.2009.09.014, IS Kyushu 2007 Special Issue on New Horizons in Earth Reinforcement.
3. Chakrabarti S, Kodikara JK, Pardo L. Survey results on stabilisation methods and performance of local government roads in Australia. *Road Transp Res*. 2002;11(3):3.
4. Lytton RL, Boggess RL, Spotts J. *Characteristics of Expansive Clay Roughness of Pavements*. Transportation Research Board; 1975.
5. Morris PH, Graham J, Williams DJ. Cracking in drying soils. *Can Geotech J*. 1992;29(2):263–277.
6. Hueckel T. On effective stress concepts and deformation in clays subjected to environmental loads: Discussion. *Can Geotech J*. 1992;29(6):1120–1125.
7. Peron H, Hueckel T, Laloui L, Hu L. Fundamentals of desiccation cracking of fine-grained soils: experimental characterisation and mechanisms identification. *Can Geotech J*. 2009;46(10):1177–1201.
8. Liu R, Vail M, Koohbor B, Zhu C, Tang C-S, Xu H, Shi X-C. Desiccation cracking in clay-bottom ash mixtures: Insights from crack image analysis and digital image correlation. *Bull Eng Geol Environ*. 2022;81(4):139.
9. Cassiani G, Brovelli A, Hueckel T. A strain-rate-dependent modified Cam-Clay model for the simulation of soil/rock compaction. *Geomech Energy Environ*. 2017;11:42–51.
10. Veveakis E, Regenauer-Lieb K. Cnoidal waves in solids. *J Mech Phys Solids*. 2015;78:231–248. http://dx.doi.org/10.1016/j.jmps.2015.02.010.
11. Konrad J-M, Ayad R. Desiccation of a sensitive clay: field experimental observations. *Can Geotech J*. 1997;34(6):929–942.
12. Costa S, Kodikara J, Shannon B. Salient factors controlling desiccation cracking of clay in laboratory experiments. *Géotechnique*. 2013;63(1):18–29.
13. Ruoyu C, Winston L, Tomasz H, Veveakis M. The physics of desiccation cracks 1: ductile fracturing and dependence on relative humidity. *Geomech Energy Environ*. 2023. http://dx.doi.org/10.1016/j.gete.2023.100488.
14. Veveakis M, Poulet T. A note on the instability and pattern formation of shrinkage cracks in viscoplastic soils. *Geomech Energy Environ*. 2021;25:100198. http://dx.doi.org/10.1016/j.gete.2020.100198.
15. Blaber J, Adair B, Antoniou A. Ncorr: open-source 2D digital image correlation matlab software. *Exp Mech*. 2015;55(6):1105–1122.
16. Das B. *Soil Mechanics: Laboratory Manual*. Oxford University Press; 2012.
17. McKenzie D. The generation and compaction of partially molten rock. *J Petrol*. 1984;25:713–765.
18. Cristescu N. *Dynamic Plasticity*. Elsevier; 2012.
19. Drew DA, Segel LA. Averaged equations for two-phase flows. *Stud Appl Math*. 1971;50(3):205–231. http://dx.doi.org/10.1002/sapm1971503205.
20. Veveakis E, Regenauer-Lieb K, Weinberg R. Ductile compaction of partially molten rocks: the effect of non-linear viscous rheology on instability and segregation. *Geophys J Int*. 2014;200(1):519–523.
21. Alevizos S, Poulet T, Sari M, Lesueur M, Regenauer-Lieb K, Veveakis M. A framework for fracture network formation in overpressurised impermeable shale: deformability versus diagenesis. *Rock Mech Rock Eng*. 2017;50(3):689–703.
22. Hill R. Acceleration waves in solids. *J Mech Phys Solids*. 1962;10(1):1–16.
23. Hueckel T, Mielniczuk B, El Youssoufi MS, Hu L, Laloui L. A three-scale cracking criterion for drying soils. *Acta Geophys*. 2014;62. http://dx.doi.org/10.2478/s11600-014-0214-9.
24. Péron H, Hueckel T, Laloui L. An improved volume measurement for determining soil water retention curves. *Geotech Test J*. 2007;30(1):1–8.
25. Tang C-S, Cui Y-J, Tang A-M, Shi B. Experiment evidence on the temperature dependence of desiccation cracking behavior of clayey soils. *Eng Geol*. 2010;114(3):261–266. http://dx.doi.org/10.1016/j.enggeo.2010.05.003.
26. Tang C-S, Shi B, Liu C, Suo W-B, Gao L. Experimental characterization of shrinkage and desiccation cracking in thin clay layer. *Appl Clay Sci*. 2011;52(1–2):69–77.
27. Tang C-S, Zhu C, Cheng Q, Zeng H, Xu J-J, Tian B-G, Shi B. Desiccation cracking of soils: A review of investigation approaches, underlying mechanisms, and influencing factors. *Earth-Sci Rev*. 2021;216:103586. http://dx.doi.org/10.1016/j.earscirev.2021.103586.
28. Reeve MJ, Hall DGM. Shrinkage in clayey subsoils of contrasting structure. *J Soil Sci*. 1978;29(3):315–323. http://dx.doi.org/10.1111/j.1365-2389.1978.tb00779.x.
29. Green DW, Southard MZ. *Perry's Chemical Engineers' Handbook*. McGraw-Hill Education; 2019.
30. Michaels AS, Lin C. Permeability of kaolinite. *Ind Eng Chem*. 1954;46(6):1239–1246.
31. Bourne N, Millett J, Rosenberg Z, Murray N. On the shock induced failure of brittle solids. *J Mech Phys Solids*. 1998;46(10):1887–1908.
32. Molinari A, Ravichandran G. Fundamental structure of steady plastic shock waves in metals. *J Appl Phys*. 2004;95(4):1718–1732.